Fabrication of micro-/nano-structured super-hydrophobic fluorinated polymer coatings by cold-spray

Kesavan Ravi, Wesley Lock Sulen, Chrystelle Bernard, Yuji Ichikawa, Kazuhiro Ogawa

Version of Record: https://www.sciencedirect.com/science/article/pii/S0257897219305675
Manuscript_373db24e34aa1c6177990e536d1b4646

Fabrication of Micro-/Nano-Structured Super-Hydrophobic Fluorinated Polymer Coatings by Cold-Spray

Kesavan Ravi[1,2,*], Wesley Lock Sulen[1], Chrystelle Bernard[1,2,3], Yuji Ichikawa[1], Kazuhiro Ogawa[1,2]

1) Fracture and Reliability Research Institute, Tohoku University, Japan

2) ELyTMaX, CNRS, Tohoku University and Université de Lyon

3) Frontier Research Institute for Interdisciplinary Sciences, Tohoku University, Japan

[*]*Corresponding author (email: kesravi16@gmail.com)*

Abstract

A fabrication of super hydrophobic Perfluoroalkoxy Alkane (PFA) coatings on stainless steel surfaces by cold-spray technique has been demonstrated in this work. The in-situ supersonic impact deposition and consolidation of finely divided 20-40 µm powder material yielded hydrophobic thin coatings of PFA which exhibited contact angles of 125^{o} but high roll off angles of 60^{o}. The deposition efficiencies were less than 0.5%, coating was mechanically very fragile and non-uniform. However, the cold-spray deposition efficiency was subsequently increased to almost 15% by performing simple modification of particle surface morphology by introducing organosilane coated nanoceramic layers on the PFA particles and by laser texturing the stainless-steel substrate surfaces to form mountain-valley micro-structures. The nanoceramic interlayers formed bridge bonds at the particle-particle interface and laser texturing achieved efficient coating-substrate interlock. The improved coatings exhibited super-hydrophobic character with 160^{o} contact angle and 6^{o} roll-off angle. The superhydrophobicity was seen to be as a result of micro-/nano-structured

surface consisting of papillae like structures capped by a layer of hydrophobic nanoceramic. The coating also exhibited excellent water repellency.

Keywords: Superhydrophobic coating; Cold spray; Polymer; PFA;

1 Introduction

Hydrophobicity is a highly sought-after functionality, in the form of coatings, on various surfaces for several applications including hydro-marine [1,2], automobile [3,4], bio-medical [5,6] etc., which require the coating application to be rapid, scalable and economical. Perfluoroalkoxy alkane (PFA) is a fluoropolymer widely known for its non-stick properties, hydrophobicity, chemical resistance, and impact resistance [7–9]. Most commonly, fluoropolymers are coated by a multi-step process involving dipping, electrostatic spray or fluidized bed coating which is followed by heat treatment for the sintering to be achieved [8–10]. The coating methods, tend to be either elaborate and expensive, skill-based, non-ecofriendly etc. Recently, cold-spray has been demonstrated to be an effective technique to fabricate polymer coatings on different substrates [11–13] by the process of supersonic impact deposition of micron-sized powder particles at high velocities and controlled temperatures. The impacting particles in the solid-state experiences an ultra-high strain rate deformation followed by various thermo-chemical transformation due to the resulting heat, pressure, plastic deformation and compressive state generated to obtain bonding at the interface [14–17]. Cold spray offers an attractive alternative for the deposition of polymers because of the following: (i) one-step rapid solid-state deposition; (ii) solventless deposition; (iii) the ability to coat large planar/non-planar objects in the field (iv) limited post-deposition processing. While cold spray has been widely commercialized for a range of materials (metals/ceramics/composites systems [15,18–21]), scarce studies are found on polymer systems. Only a handful of studies can be found, of which, Ravi et al [12–14,22] reported the possibility of cold-spray being used to coat Ultra-High Molecular Weight Polyethylene, whereas Alhulaifi et al. [23] used High

Density Polyethylene (HDPE), Xu et al. [24] used polyolefin powders and Bush et al. [25] used BYK Ceraflour showing that cold-spray has a high potential for being a fast, scalable, solventless and economical coating technique for polymers. However, the progress is heavily impeded by the low deposition efficiencies of the coating process.

Layer by layer depositions of polymers by cold-spray majorly involve, the (i) spray particle impact bonding with substrate and, (ii) spray particle impact bonding with the already deposited layer. In the case (i), several works have suggested the importance of modifying substrate topography by laser patterning to increase the coating-substrate adhesion by mechanical anchorage [26,27]. The controlled ablation technique of lasers allows modification to be performed to the desired topology without the risk of micro-crack nucleation or chemical modifications to the surface [27]. Whereas, in the case (ii), previous works have highlighted the improvement in the coating efficiencies by the use of nano-ceramic interlayers at the particle-substrate and particle-particle interfaces by the formation of bridge bonds at the bonding interfaces [13,14,22,28].

Hence, this research work demonstrates the fabrication of superhydrophobic PFA coatings by cold-spray technique in a step-by-step manner and then demonstrating the hydrophobicity of the obtained coatings. The research work first reports on the coating formation and its characteristics when a downstream injection cold spray is used to coat PFA on as-received stainless-steel (SUS 304) substrates. The work then reports on the consequences of modifying the bonding interfaces, namely particle-particle and particle-substrate interfaces by introducing nanoceramic interlayers and by laser texturing the substrate surfaces to increase the deposition efficiency of PFA coating. The hydrophobic character of the coatings with and without the bonding interface enhancement is compared

and contrasted by contact angle, roll-off angle and dynamic water droplet impact measurements. The deposition characteristics and the microstructure of the resultant coating were analyzed, and the mechanism of water repellency is discussed using a 2D mathematical model for wetting.

2 Experimental

2.1 Powder Materials

Two kinds of powder feedstock were prepared for cold spray. The first kind of powder was the polymer Perfluoroalkoxy alkane (PFA) procured from Daikin, Japan available under the product name NEOFLON PFA. The powder consisted of a distribution of 20-40 μm particles as shown in figure 1(a). The second kind of powder feedstock consisted of micron sized PFA polymer particles with nanoceramics particles dispersed on its surface forming a core-shell arrangement as shown in the figure 1(b). The nanoceramics used is Fumed Nano Alumina (FNA) powder of 7-20 nm primary particle size procured from Evonik Industries, Japan available under the product name AEROXIDE ® ALU C 805. The FNA is highly hydrophobized with organosilane [29–31]. For preparing the core-shell structure, the PFA powder was mixed with 5% (by weight) FNA powder in an ethanol bath by ultrasound mixing for 30 mins and dried off in air for 24 hours to completely remove any traces of ethanol left. Table 1 shows the physical properties of the feedstock materials.

Table 1 The physical properties of the feedstock material

Powder Material	Particle Size	Melting Temperature	Specific Surface Area
PFA	20 – 60 μm	576 – 586 K	-
FNA	7 – 20 nm	2015 – 2072 K	85 – 115 m^2/g

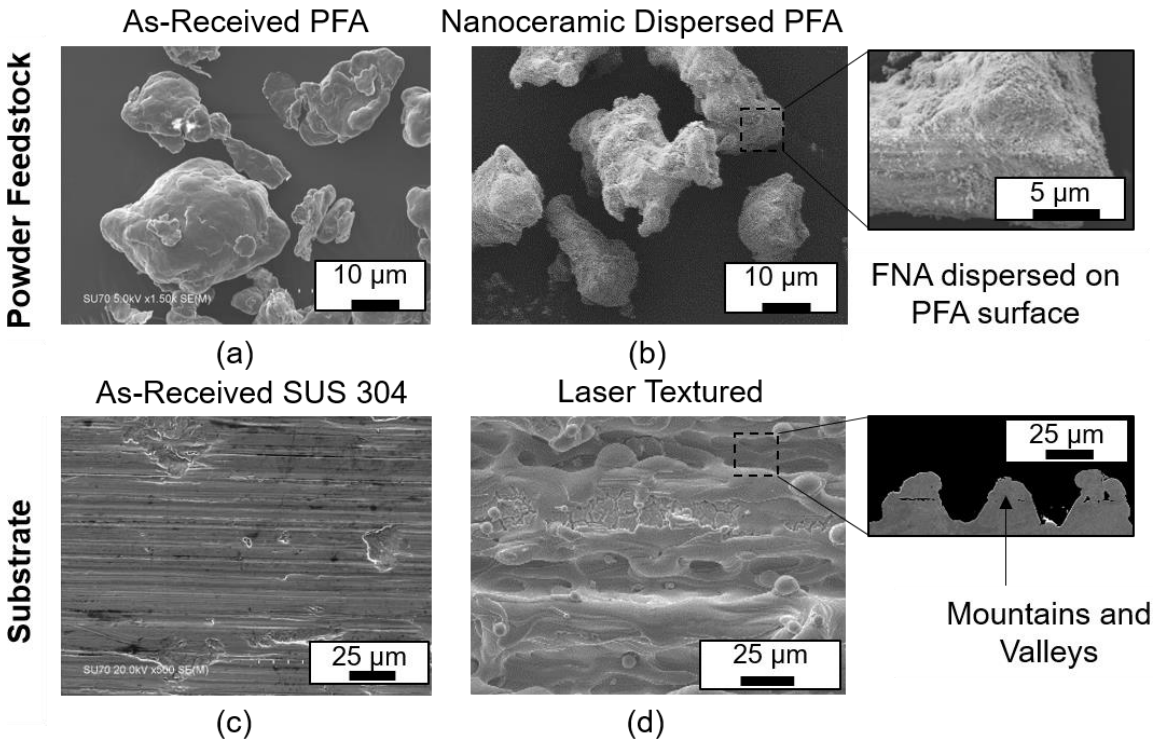

Figure 1 (a,b) SEM image of the as-received and the nanoceramic dispersed PFA powder. (c,d) SEM image of the as-received and the laser textured SUS 304 substrate surface.

2.2 Substrate

The substrates used were SUS 304 with two kinds of surface preparation: (i) as-received SUS 304 and (ii) laser textured SUS 304. The SEM image of the as-received substrate and the laser textured surface is as shown in the figure 1(c) and 1(d) respectively. The texturing of the surfaces was performed at Hakuto Industries, Japan in which a YLR-300 (air-cooled) continuous wave laser (wavelength of 1064 nm) manufactured by IPG Photonics with a SQUIRREL^{TM} scan head was used. The scan head was supplied with power and controlled by Arges System Controller (ASC-1 model). A laser output of 141.7 W with a spot diameter of 12 µm was used to perform a scanning pattern of parallel running single lines with a pitch of 50 µm at a scanning speed of 10000 mm/s. Table 2 shows the laser

parameters used to texture the stainless-steel substrates in this study. The laser scanning resulted in the formation mountain and valley patterns running across the surface as shown in inset of figure 1(d). The tips of the mountains were spaced 30-40 µm from each other and the valleys were designed to have a depth of 20-30 µm.

Table 2 The laser parameters used in this study

Laser	YLR-300-AC(air-cooled), CW, 1064nm, Manufactured by IPG
Controller	ASC-1 Model; Squirrel Manufactured by ARGES
Lens	F-θ: F100, Working Distance:87 mm
Scanning Speed	10000 mm/s
Pitch	50 µm
Laser Output	141.7 W
Spot Diameter	12 µm

2.3 Processing parameters

The cold-spray was performed with a downstream injection low pressure cold spray system available under the name Dymet 403 (Obninsk Centre for Powder Spraying, Russia). Compressed air, used as the carrier gas at a stagnant gas temperature ranging from of RT to 500^{o}C and gas pressure of 0.4 MPa, was passed through a converging-diverging (CD) nozzle with a diverging section of length 120 mm. The powder particles were fed downstream of the CD section by a vibratory feeder at a steady, controllable rate. The powder particles were heated and accelerated by the carrier gas and sprayed on the substrate surface. The spray was performed for two passes at a stand-off distance of 10 mm

by moving the sample stage perpendicular to the spray direction at a traverse speed of 50 mm/s. The schematic of the cold-spray system is shown in figure 2. The deposition efficiency (DE) calculations were performed by calculating the ratio of the mass of the powder deposited on a given substrate to the mass of the sprayed powder.

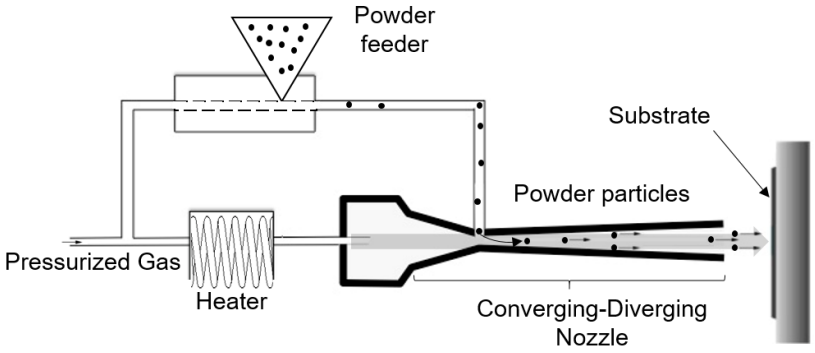

Figure 2 Schematic of the downstream injection low pressure cold-spray system.

2.4 Morphological and structural characterization

The morphological investigations were performed using a field emission scanning electron microscope (FE-SEM, Hitachi SU-70), operated at 5 kV. A thin carbon coating was applied before SEM observation by vapor deposition. The x-ray diffraction (XRD) was conducted using Cu-K_α at 40 kV/30 mA over range of 10^o-80^o (Shimadzu Scientific Instruments XRD-7000). The surface roughness parameters of the coated surface were measured by a surface roughness profilometer of the make Surfcorder SE300 by Kosaka Laboratory Ltd. The surface roughness profile and various other roughness parameters, based on the literature [32], such as average surface roughness (R_a), the root mean square surface roughness (R_q), mean spacing of profile irregularities (R_{sm}) and average maximum height of the profile (R_z) were measured and their possible relation with the wettability is discussed.

2.5 Hydrophobic character assessment

The hydrophobicity of the coating was characterized from contact angle, roll-off angle (tilting sample stage at 1^{o}/s until the first movement of water droplet) and dynamic droplet impact measurements. The contact angle and the roll-off angles were measured using a contact angle/surface tension meter of make Kyowa Interface Science Company Limited. The dynamic water droplet impact tests on the surface were video recorded with an EOS 70D Canon Digital single-lens reflex camera (DSLR) camera equipped with a macro lens (1:1 magnification) at 60 fps.

3 Results and Discussion

3.1 PFA coating by cold-spray

The spray conditions were empirically optimized based on whether or not a sound coating was formed. At low chamber temperatures, not only no coating was observed, but the substrate surface was continuously shot blasted by the impacting polymer particles. However, as the chamber temperature was increased from room temperature to 500^{o}C, the deposition efficiency increased from almost zero to 0.5%. The coating formed was a non-uniform layer with a thickness approximately around 2-5 µm. Figure 3(a) and (b) shows the top view SEM images and figure 3(c) the XRD of the PFA coating on SUS 304 substrate when sprayed at the conditions corresponding to a chamber gas temperature of 500^{o}C and a gas pressure of 0.4 MPa. The XRD data showed that the positions of peaks obtained from the coating can be matched with that of the PFA powder, confirming the presence of the coating. Figure 3 (b) shows the non-uniform deposition of the PFA coating on the SUS 304 substrate.

The low deposition efficiency can be traced back to the low surface energy of fluoropolymers [9] in general because of which fluoropolymeric particles tend to fail in bonding with the substrate surface during the impact deformation. However, the small increase in the deposition efficiency with the increase in the gas temperature can be because of the apparent softening of the polymeric particle at higher temperatures and its decrease in the elastic strain energy which helps the impacting polymer to have a decreased tendency to rebound. This phenomenon has also been similarly observed by Ravi et al. [14] for another low surface energy material called Ultra-High Molecular Weight Polyethylene (UHMWPE) in similar impacting conditions. A likely consequence of such depositions is a very low adhesion strength which has been seen in the case of PFA coatings. The coating showed a very low adhesion strength with the substrate surface and can be readily peeled off by hand. As the mechanical strength and the practical usability of such coatings was rather limited, efforts were made to enhance the coating quality by focusing on ways to enhance the bonding strength at particle-particle and the coating-substrate interfaces.

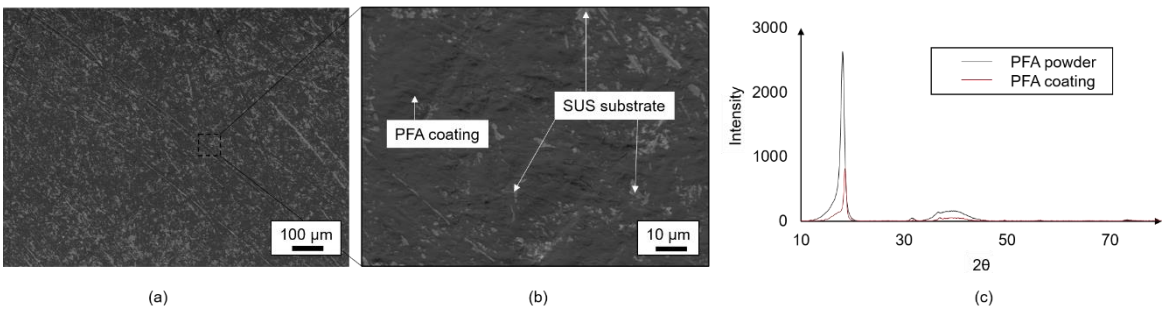

Figure 3 (a,b) The SEM images of the coated surface in top view at different magnifications. The darker regions indicate the coated material and the lighter areas indicate the SUS substrate (c) The XRD of the powder and the PFA coating.

3.2 Enhanced PFA-FNA coatings by cold-spray

Cold-spray was performed with powder feedstock which consisted of PFA polymer particles with FNA particles dispersed on its surface forming a core-shell arrangement as shown in the figure 1(b). The motivation to disperse FNA particles on the feedstock PFA powder particles were two fold. Firstly, the FNA particles were intended to form strong mechanical bridge bonds at the particle-particle interface which has been also demonstrated by Ravi et al [12,13] for cold-sprayed coatings with UHMWPE. Secondly, the FNA, used here, is also highly hydrophobized with organosilane which could contribute to the overall hydrophobicity of the coating as it is present at the coating surface. The second important enhancement performed was to increase the coating-substrate interface strength. Several kinds of literature suggested that coating-substrate interfaces were significantly strengthened by increasing the substrate surface roughness before coating, roughening either by abrasive paper or shot blasting [33–36]. In this study, however, the substrates were laser textured to a defined pattern which has already been described in the section 2.2. The dimensions of the mountains and valleys and their spacing, which were approximately within the range of 20-40 µm, were fabricated to be as close to dimensions of the sprayed particle size.

Figure 4 (a) shows the illustration of the impact of core-shell PFA-FNA particle on the laser textured SUS 304 surface and figure 4(b) and 4(c) respectively shows the SEM cross-section and the top view of the actual coating. The coating was fabricated by the processing parameters corresponding to a chamber gas temperature of 500^{o}C and a gas pressure of 0.4 MPa which yielded a uniform coating thickness of 200 µm. The resultant coating is confirmed from the XRD data in figure 4 (d) in which the positions of the peak for the PFA-FNA coating matched with the PFA-FNA feedstock powder. Such coatings were

possible to be fabricated at great processing speeds which, in this case, was achieved in only about 30 s-1 min of spray deposition on a substrate surface of 0.1 m^2. The introduction of the FNA as an interlayer coupled with the laser texturing of substrate surface yielded improved coatings of deposition efficiency as high as 15% (the highest reported efficiency in the literature is 5% [11]).

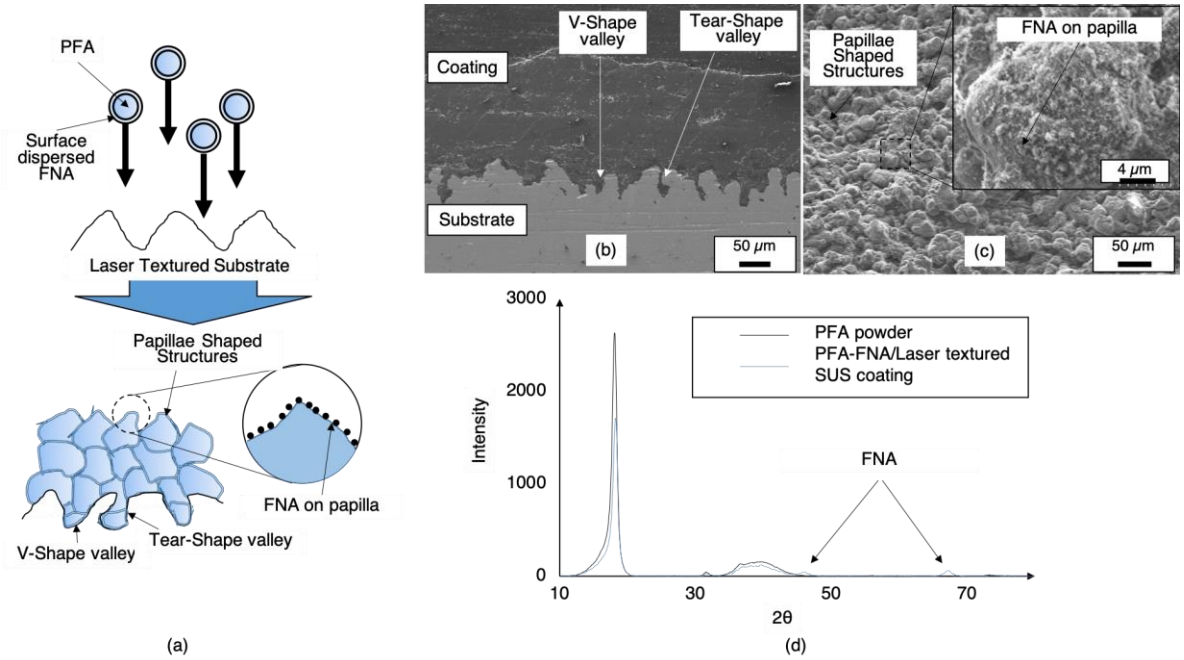

Figure 4 (a) Illustration of the impact of powder feedstock which consisted of PFA polymer particles with FNA particles dispersed on its surface forming a core-shell arrangement and coating formation on the laser textured SUS 304 surface. (b) The SEM image of the cross section and (c) the surface topology of PFA-FNA coating on the laser textured substrate. (4 (c) Inset: Magnified SEM image of a papillae-like structure). (d) The XRD of the powder and the PFA-FNA coating

The cross-section of the PFA coated surface on SUS 304 surface is as shown in the figure 4(b). The coating-substrate interface shows the effective interlock formed by the laser

textured narrow mountains and valleys effectively pinning the coating to the substrate. On close examination, the interface revealed the effective entrapment of the impacted polymer particles by the tight V-shaped and tear-shaped valleys which is conjectured to be critical in achieving the high deposition efficiency. Moreover, the coating-substrate interface showed little to no gaps between PFA and the substrate surface. The coating volume of PFA-FNA showed a very dense microstructure and good mechanical strength. A preliminary analysis of durability of the coating was performed under a 15 m/s water jet in which the coating held up without delamination. However, an in-depth mechanical analysis as well as the detailed study on the effect of FNA on reinforcing is underway and will be reported as an independent study.

The top view of the coating is shown in the figure 4(c) showing the microstructure of the coated surface comprising of papilla shaped PFA capped with a layer of hydrophobic FNA (figure 4(c) inset) forming a double structure (much like the case seen on a lotus leaf [37]). The papillae-like structures were seen to be 10-20 μm in height and width on an average. The formation of the V-shaped and tear-shaped valleys and the papillae-like structures formed on the coated surface as illustrated in figure 4(a). The same structures are evidenced by the SEM images of the coating as shown in figure 4(b) and 4(c).

3.3 Characterization of the wetting behavior

Wetting behavior of the coatings were tested by water contact angle, roll-off angle and dynamic water droplet impact measurements. For the water contact angle measurements, a 3 μL droplet was gently placed on the coated surface at five random locations and contact angle was measured. For the roll-off angle measurements, a 20 μL droplet was placed on the substrate and the sample stage was slowly tilted and five iterations were performed to

ensure repeatability. Dynamic water impact tests were also carried out to understand the water repellency of the coating. Water droplet of size 2 mm was dropped on to the coated surface and impacted at a velocity of 2.5 m/s. The impact and rebound of the water droplet were recorded using a 60 fps DSLR camera.

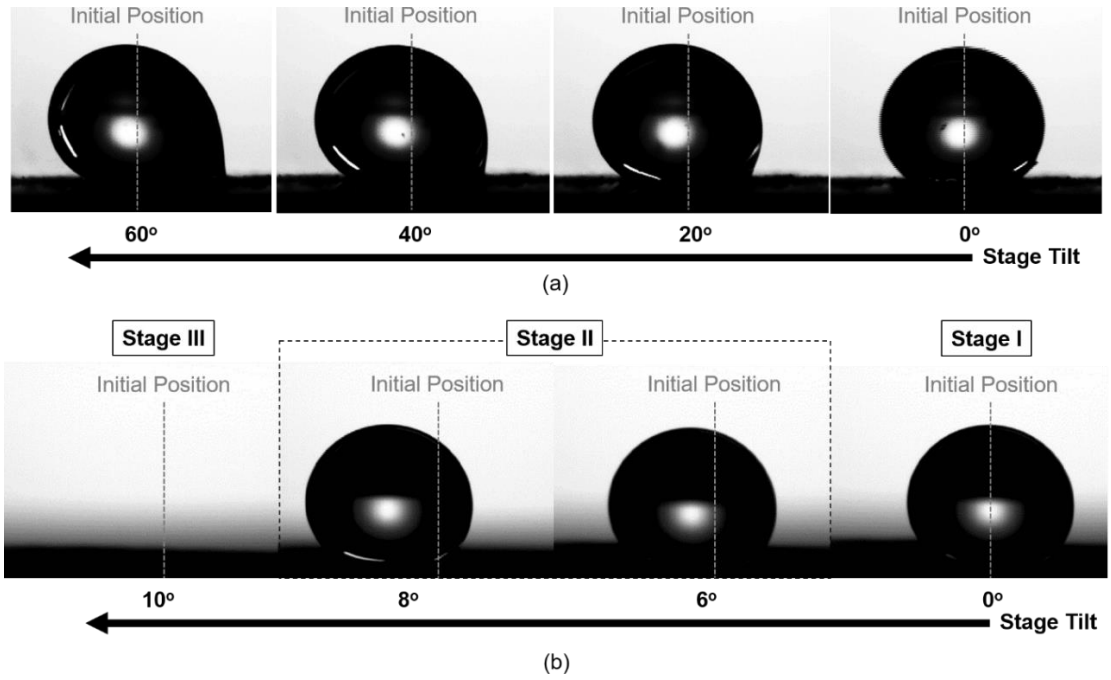

Figure 5 Water roll-off measurement on the (a) PFA coatings on SUS 304 substrate and (b) PFA-FNA coating on laser textured SUS 304 substrate.

Both the coatings, namely PFA and the PFA-FNA coatings showed hydrophobicity. The PFA coating showed contact angles of up to 125 ± 10^{o}. The high dispersion in the values were due to the non-uniformity in the coverage of the coating over the substrate surface. Areas covered by the PFA showed contact angles close to 130^{o}. Other areas exhibited a contact angle close to 115^{o}. The coatings exhibited roll-off angles of more than 60^{o}. The travel of the water droplet was not smooth which can be again attributed to the non-uniformity of the coating. Additionally, the droplets exhibited increasing amount of

hysteresis for successively higher tilt angles. The varying droplet behavior at increasing stage tilt angles is shown in figure 5(a). Figure 6 shows the water contact angle and the roll off angles shown by the PFA coatings.

On the other hand, the PFA-FNA coatings on the laser textured SUS 304 substrates showed superhydrophobicity exhibiting contact angles as high as 160 ± 3^{o}. The coated surface also exhibited excellent roll-off angles of 6^{o}. The high contact angle greater than 150^{o} and low roll-off angle less than 10^{o} classify this wetting behavior as super-hydrophobic [38]. The figure 5(b) shows three stages of the water droplet during the tilt: (i) static droplet at 0^{o} of stage tilt; (ii) droplet displaced from the original position at 6^{o} of stage tilt; (iii) the stage with droplet rolled off. It has to be noted that the water droplet showed minimal hysteresis indicating an excellent mobility of the droplet. Figure 6 shows the water contact angle and the roll off angles shown by the PFA-FNA coatings on the laser textured SUS 304 substrates.

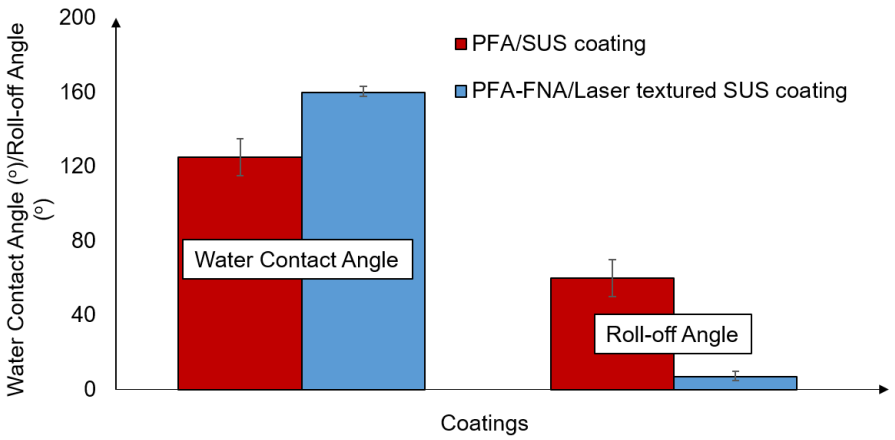

Figure 6 The water contact angle and the roll off angles shown by the PFA coatings on SUS 304 substrates and the PFA-FNA coatings on the laser textured SUS 304 substrates.

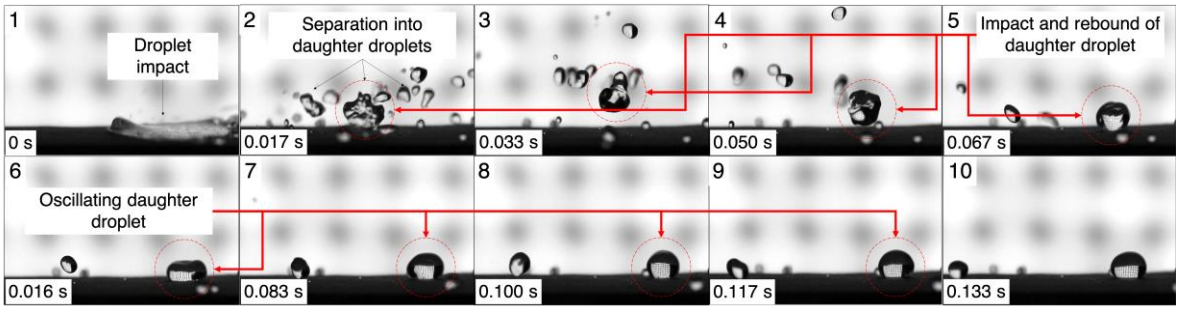

Figure 7 Dynamic water impact testing on PFA-FNA coatings on laser textured SUS 304 substrates.

The dynamic water droplet impact testing was performed on PFA-FNA coatings and a video of the impact process was recorded. The frames extracted from the video is as shown in the figure 7. It was observed that the water droplet upon impact rebounded completely and separated into several daughter droplets. These daughter droplets proceeded to rebound several times and oscillated a few times before coming to a standstill. These aspects of the water droplets on the coated surface demonstrate excellent water repellency of the coating.

3.3.1 Surface Microstructure and hydrophobicity

The PFA coating was seen to be moderately hydrophobic. However, the roll-off angles exhibited were clearly high which limited the water mobility on the surface. The wetting behavior on such surface can be attributed to the smooth yet non-uniformly covered coated surface. Figure 8(a) shows the surface roughness profile of the PFA coating on SUS. It can be clearly seen that the surface consists of mostly smooth surface with occasional mountain structures. The average roughness (R_a) and the root mean square surface roughness (R_q) measured were 2.132 µm and 2.133 µm which was quite low compared to that of the PFA-FNA coatings.

On the other hand, PFA-FNA coatings on laser textured SUS exhibited superhydrophobicity exhibiting high contact angles 160 ± 3^{o} which was ~40-45% higher than the contact angle measured on a smooth PFA surface [39] or Teflon tape [40]. The root of the such a wetting character on the PFA-FNA coating can be traced to the combination of three phenomena:

(i) Inherent low surface energy and hydrophobicity of PFA [8,39] and FNA [29–31];

(ii) High surface roughness (R_a=8.211 µm; R_q=10.247 µm) which is considerably higher than for PFA coatings on SUS as shown in figure 8 (a). The list of all the roughness parameters (R_a, R_q, R_{sm} and R_z), is given in the table 3.

(iii) Double structure by the papillae-like formation and the fine FNA particles on these papillae.

Table 3 The list of the surface roughness parameters of the coatings used in this study

Roughness Parameter / Coating	R_a (µm)	R_q (µm)	R_{sm} (mm)	R_z (µm)
PFA coating on SUS	2.132±1.483	2.887±1.725	0.178±0.058	14.301±6.721
PFA-FNA coating on Laser Textured SUS	8.211±0.947	10.247±1.142	0.199±0.013	47.298±4.068

Hence, the water droplets ended up resting on the tips of the FNA coated PFA mountains forming a stable superhydrophobic structure. These characteristics contributed to the

excellent water repellence and mobility of the coating by decreasing the actual contact area between the water droplet surface and the coating as well as by facilitating the formation of micro air pocket.

The observed effects are consistent with the Wenzel and Cassie-Baxter wetting models which suggests that the surface roughness, inherent hydrophobicity and double structure can amplify the effect of water contact angle on a surface [41,42]. The Wenzel equation (equation 1) can be used to predict the evolution of the water contact angle with the increase in the roughness in a homogenous wetting regime. The equation states, θ_w, which is the measured water contact angle corresponding to the stable equilibrium state will vary as follows:

$$cos\theta_w = rcos\theta_Y \quad (1)$$

The roughness factor, *r*, which is the measure of ratio of the true area to the apparent area. Here an approximate value of *r*, is obtained by calculating the ratio of the length of the line tracing the roughness profile to the projected length of the line and was determined to be 1.15 for the PFA coating and 1.65 PFA-FNA coating. θ_Y, which is the contact angle of water droplet on an ideally smooth PFA surface is around 110^o [39].

In a heterogeneous wetting regime, the contact angle can be explained using Cassie-Baxter equation [41] (equation 2), which states:

$$cos\theta_w = r \times f \times cos\theta_Y + f - 1 \quad (2)$$

Where f is the fraction of the solid surface wet by the liquid.

A simple 2D mathematical model is illustrated in figure 8(b) and (c). Based on the surface roughness measurement, the PFA coating and the PFA-FNA coatings are represented as a

simple saw-tooth surface with the geometrical parameters constructed from the R_z and R_{sm} values. As shown in the figure 8 (b) and (c), when water was placed on the PFA coating, the droplet is assumed to exhibit Wenzel state of wetting and for the PFA-FNA coating, it is assumed to be a Cassie-Baxter wetting state in which air was trapped between the teeth and the water penetrated into the gaps to some depth [43]. Incorporating these features, the calculated θ_w for PFA coating was 115^o and θ_w for the PFA-FNA coating was 155^o which was very close to the experimentally calculated water contact angles.

Hence, the 2D mathematical model provided a first-approach yet significant understanding of the wetting behavior of the PFA coatings and PFA-FNA coatings

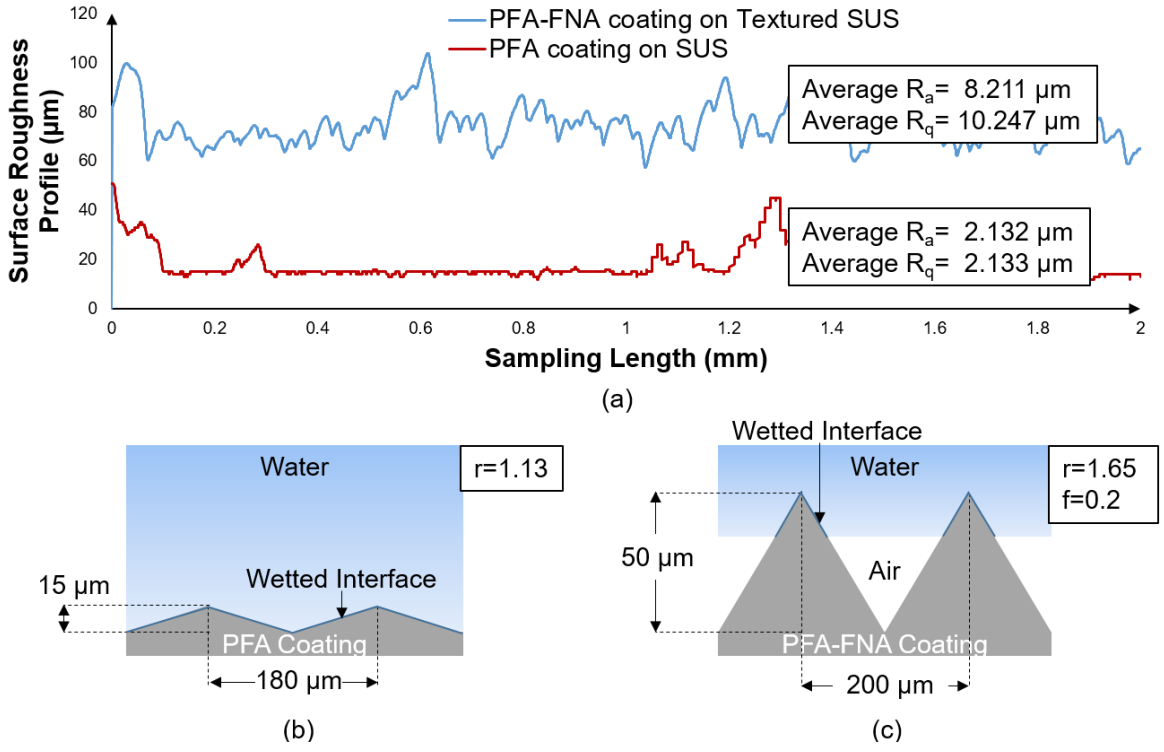

Figure 8 (a) The surface roughness profile of the PFA coating and PFA-FNA coating. (b,c) The schematic of the saw-tooth geometry representing the roughness of PFA and PFA-FNA coating respectively and the interaction of the water droplet with the rough interfaces.

4 Conclusions

In summary, superhydrophobic PFA coatings were fabricated by a one-step, rapid, scalable, and solventless technique called cold-spray by in-situ supersonic impact deposition and consolidation. The processing parameters were optimized to obtain PFA coatings on SUS substrates which exhibited contact angles of 125^{o}. The coatings were not only extremely fragile and non-uniform coatings of extremely low deposition efficiencies (less than 0.5%) but it also exhibited a high roll-off angles of ~60^{o}. The wetting behavior on such surface can be attributed to the smooth yet non-uniformly covered coated surface. Subsequently, high deposition efficiency coatings as high as 15% were achieved by adding FNA nanoceramic interlayers at the bonding interfaces and laser texturing the surface to achieve efficient coating-substrate interlock. The PFA-FNA coatings exhibited superhydrophobicity with contact angle up to 160^{o}, roll-off angle of 6^{o} and excellent water repellency to dynamic water droplet impacts. The superhydrophobicity was seen to be as a result of micro/nano double structured surface consisting of papillae like structured capped by a hydrophobic nanoceramic layers, high roughness of the coatings and the inherent low surface energy and hydrophobicity of PFA and FNA. The 2D mathematical model used in the study predicted the experimental water contact angle from the roughness features in the coating. This research indicates that cold-spray is an efficient, scalable and rapid method to fabricate super hydrophobic coatings in large scale.

Acknowledgments

This work was partly supported by JSPS KAKENHI Grant-in-Aid for Scientific Research (A) 17H01235. Authors would like to acknowledge JSPS for the research grant as the corresponding author is a postdoctoral JSPS Research Fellow.

References

[1] J.A. Callow, M.E. Callow, Trends in the development of environmentally friendly fouling-resistant marine coatings, Nat. Commun. 2 (2011) 244.

[2] J. Genzer, K. Efimenko, Recent developments in superhydrophobic surfaces and their relevance to marine fouling: a review, Biofouling. 22 (2006) 339–360.

[3] J.C. Thies, G.J.W. Meijers, J.A. Pitkin, E. Currie, C.F. Tronche, J.E. Southwell, Hydrophobic coatings comprising reactive nano-particles, (2006).

[4] Y. Taga, Recent progress in coating technology for surface modification of automotive glass, J. Non. Cryst. Solids. 218 (1997) 335–341.

[5] Q. Wei, R. Haag, Universal polymer coatings and their representative biomedical applications, Mater. Horizons. 2 (2015) 567–577.

[6] H.J. Busscher, I. Stokroos, H.C. der Mei, P.G. Rouxhet, J.M. Schakenra Ad, Preparation and characterization of superhydrophobic FEP-teflon surfaces, J. Adhes. Sci. Technol. 6 (1992) 347–356.

[7] L.M. Siperko, R.R. Thomas, Chemical and physical modification of fluoropolymer surfaces for adhesion enhancement: a review, J. Adhes. Sci. Technol. 3 (1989) 157–173.

[8] E. Leivo, T. Wilenius, T. Kinos, P. Vuoristo, T. Mäntylä, Properties of thermally sprayed fluoropolymer PVDF, ECTFE, PFA and FEP coatings, Prog. Org. Coatings. 49 (2004) 69–73.

[9] H.I. Rowan, Thermoplastic fluoropolymers, ASM Int. Eng. Plast. Eng. Mater. Handbook,. 2 (1988) 115–119.

[10] E. Celia, T. Darmanin, E.T. de Givenchy, S. Amigoni, F. Guittard, Recent advances in designing superhydrophobic surfaces, J. Colloid Interface Sci. 402 (2013) 1–18.

[11] Z. Khalkhali, W. Xie, V.K. Champagne, J.-H. Lee, J.P. Rothstein, A comparison of cold spray technique to single particle micro-ballistic impacts for the deposition of polymer particles on polymer substrates, Surf. Coatings Technol. 351 (2018) 99–107.

[12] K. Ravi, Y. Ichikawa, T. Deplancke, K. Ogawa, O. Lame, J.Y. Cavaille, Development of Ultra-High Molecular Weight Polyethylene (UHMWPE) Coating by Cold Spray Technique, J. Therm. Spray Technol. 24 (2015) 1015–1025. doi:10.1007/s11666-015-0276-5.

[13] K. Ravi, Y. Ichikawa, K. Ogawa, T. Deplancke, O. Lame, J.Y. Cavaille, Mechanistic

Study and Characterization of Cold-Sprayed Ultra-High Molecular Weight Polyethylene-Nano-ceramic Composite Coating, J. Therm. Spray Technol. 25 (2016) 160–169. doi:10.1007/s11666-015-0332-1.

[14] K. Ravi, T. Deplancke, K. Ogawa, J.-Y. Cavaillé, O. Lame, Understanding deposition mechanism in cold sprayed ultra high molecular weight polyethylene coatings on metals by isolated particle deposition method, Addit. Manuf. (2018). doi:https://doi.org/10.1016/j.addma.2018.02.022.

[15] V.K. Champagne, The cold spray materials deposition process Fundamentals and applications, Elsevier, 2007. doi:10.1533/9781845693787.frontmatter.

[16] H. Assadi, F. Gärtner, T. Stoltenhoff, H. Kreye, Bonding mechanism in cold gas spraying, Acta Mater. 51 (2003) 4379–4394.

[17] S. Guetta, M.-H. Berger, F. Borit, V. Guipont, M. Jeandin, M. Boustie, Y. Ichikawa, K. Sakaguchi, K. Ogawa, Influence of particle velocity on adhesion of cold-sprayed splats, J. Therm. Spray Technol. 18 (2009) 331–342.

[18] A. Moridi, S.M. Hassani-Gangaraj, M. Guagliano, M. Dao, Cold spray coating: review of material systems and future perspectives, Surf. Eng. 30 (2014) 369–395.

[19] M.F. Smith, J.E. Brockmann, R.C. Dykhuizen, D.L. Gilmore, R.A. Neiser, T.J. Roemer, Cold Spray Direct Fabrication – High Rate, Solid State, Material Consolidation, MRS Proc. 542 (1999) 65–76.

[20] A. Papyrin, V. Kosarev, S. Klinkov, A. Alkhimov, V.M. Fomin, Cold Spray Technology, 2007. doi:10.1016/B978-0-08-045155-8.X5000-5.

[21] P. Matteazzi, A. Colella, V. Leshchynsky, K. Sakaki, H. Fukanuma, R.G. Maev, Cold Spray Powders and Equipment, in: Cold Gas Dyn. Spray, CRC Press, 2016: pp. 81–144.

[22] J.-Y. Cavaille, L. Olivier, T. Deplancke, K. Ogawa, R. Kesavan, Powder for cold spray, method for manufacturing macromolecular coating film, and macromolecular coating film, (2015).

[23] A.S. Alhulaifi, G.A. Buck, W.J. Arbegast, Numerical and experimental investigation of cold spray gas dynamic effects for polymer coating, J. Therm. Spray Technol. 21 (2012) 852–862.

[24] Y. Xu, I.M. Hutchings, Cold spray deposition of thermoplastic powder, Surf. Coatings Technol. 201 (2006) 3044–3050.

[25] T.B. Bush, Z. Khalkhali, V. Champagne, D.P. Schmidt, J.P. Rothstein, Optimization of Cold Spray Deposition of High-Density Polyethylene Powders, J. Therm. Spray

Technol. 26 (2017) 1548–1564.

[26] P. Fauchais, A. Vardelle, M. Vardelle, M. Fukumoto, Knowledge concerning splat formation: an invited review, J. Therm. Spray Technol. 13 (2004) 337–360.

[27] R. Kromer, S. Costil, J. Cormier, D. Courapied, L. Berthe, P. Peyre, M. Boustie, Laser surface patterning to enhance adhesion of plasma sprayed coatings, Surf. Coatings Technol. 278 (2015) 171–182.

[28] K. Ravi, Y. Ichikawa, K. Ogawa, T. Deplanke, O. Lame, J.-Y. Cavaille, Mechanistic study and characterization of cold sprayed ultra high molecular weight polyethylene-nano ceramic composite coating, in: Proc. Int. Therm. Spray Conf., 2015.

[29] C. Lin, D.D.L. Chung, Nanostructured fumed metal oxides for thermal interface pastes, J. Mater. Sci. 42 (2007) 9245–9255.

[30] B.W. Zewde, S. Admassie, J. Zimmermann, C.S. Isfort, B. Scrosati, J. Hassoun, Enhanced Lithium Battery with Polyethylene Oxide-Based Electrolyte Containing Silane--Al2O3 Ceramic Filler, ChemSusChem. 6 (2013) 1400–1405.

[31] R. Riedel, L. Toma, C. Fasel, G. Miehe, Polymer-derived mullite--SiC-based nanocomposites, J. Eur. Ceram. Soc. 29 (2009) 3079–3090.

[32] M. Miwa, A. Nakajima, A. Fujishima, K. Hashimoto, T. Watanabe, Effects of the surface roughness on sliding angles of water droplets on superhydrophobic surfaces, Langmuir. 16 (2000) 5754–5760.

[33] A.F. Harris, A. Beevers, The effects of grit-blasting on surface properties for adhesion, Int. J. Adhes. Adhes. 19 (1999) 445–452.

[34] R. Maboudian, R.T. Howe, Critical review: Adhesion in surface micromechanical structures, J. Vac. Sci. Technol. B Microelectron. Nanom. Struct. Process. Meas. Phenom. 15 (1997) 1–20.

[35] J.J. BIKERMAN, The Science of Adhesive Joints, Acad. Press. New-York London. (1961) 1961. doi:10.1016/0021-9797(69)90392-0.

[36] D. Taylor, J.E. Rutzler, Adhesion Using Molecular Models. Adhesion of Polyethylene and Poly (vinyl Chloride) to Metals, Ind. Eng. Chem. 50 (1958) 928–934.

[37] C. NEINHUIS, W. BARTHLOTT, Characterization and Distribution of Water-repellent, Self-cleaning Plant Surfaces, Ann. Bot. 79 (1997) 667–677. doi:10.1006/anbo.1997.0400.

[38] M. Ma, R.M. Hill, Superhydrophobic surfaces, Curr. Opin. Colloid Interface Sci. 11

(2006) 193–202.

[39] O.M. Magens, Y. Liu, J.F.A. Hofmans, J.A. Nelissen, D.I. Wilson, Adhesion and cleaning of foods with complex structure: Effect of oil content and fluoropolymer coating characteristics on the detachment of cake from baking surfaces, J. Food Eng. 197 (2017) 48–59.

[40] J. Zhang, J. Li, Y. Han, Superhydrophobic PTFE surfaces by extension, Macromol. Rapid Commun. 25 (2004) 1105–1108.

[41] A. Marmur, Wetting on hydrophobic rough surfaces: to be heterogeneous or not to be?, Langmuir. 19 (2003) 8343–8348.

[42] G.I. Loeb, M.E. Schrader, Modern approaches to wettability: theory and applications, Springer Science & Business Media, 2013.

[43] S. Pan, R. Guo, W. Xu, Investigating and biomimicking the surface wetting behaviors of ginkgo leaf, Soft Matter. 10 (2014) 8800–8803.

Table 1 The physical properties of the feedstock material

Powder Material	Particle Size	Melting Temperature	Specific Surface Area
PFA	20 – 60 μm	576 – 586 K	-
FNA	7 – 20 nm	2015 – 2072 K	85 – 115 m^2/g

Table 2 The laser parameters used in this study

Laser	YLR-300-AC(air-cooled), CW, 1064nm, Manufactured by IPG
Controller	ASC-1 Modle; Squirrel Manufactured by ARGES
Lens	F-θ: F100, WD:87mm
Scanning Speed	10000 mm/s
Pitch	50 μm
Laser Output	141.7 W
Spot Diameter	12 μm

Table 3 The list of the surface roughness parameters of the coatings used in this study

Roughness Parameter / Coating	R_a (μm)	R_q (μm)	R_{sm} (mm)	R_z (μm)
PFA coating on SUS	2.132±1.483	2.887±1.725	0.178±0.058	14.301±6.721
PFA-FNA coating on Laser Textured SUS	8.211±0.947	10.247±1.142	0.199±0.013	47.298±4.068

List of figure captions

No.	Figure Caption
1	(a,b) SEM image of the as-received and the nanoceramic dispersed PFA powder. (c,d) SEM image of the as-received and the laser textured SUS 304 substrate surface.
2	Schematic of the downstream injection low pressure cold-spray system.
3	(a,b) The SEM images of the coated surface in top view at different magnifications. The darker regions indicate the coated material and the lighter areas indicate the SUS substrate (c) The XRD of the powder and the PFA coating.
4	(a) Illustration of the impact of powder feedstock which consisted of PFA polymer particles with FNA particles dispersed on its surface forming a core-shell arrangement and coating formation on the laser textured SUS 304 surface. (b) The SEM image of the cross section and (c) the surface topology of PFA-FNA coating on the laser textured substrate. (4 (c) Inset: Magnified SEM image of a papillae-like structure). (d) The XRD of the powder and the PFA-FNA coating
5	Water roll-off measurement on the (a) PFA coatings on SUS 304 substrate and (b) PFA-FNA coating on laser textured SUS 304 substrate.
6	The water contact angle and the roll off angles shown by the PFA coatings on SUS 304 substrates and the PFA-FNA coatings on the laser textured SUS 304

	substrates.
7	Dynamic water impact testing on PFA-FNA coatings on laser textured SUS 304 substrates.
8	(a) The surface roughness profile of the PFA coating and PFA-FNA coating. (b,c) The schematic of the saw-tooth geometry representing the roughness of PFA and PFA-FNA coating respectively and the interaction of the water droplet with the rough interfaces.

Figures

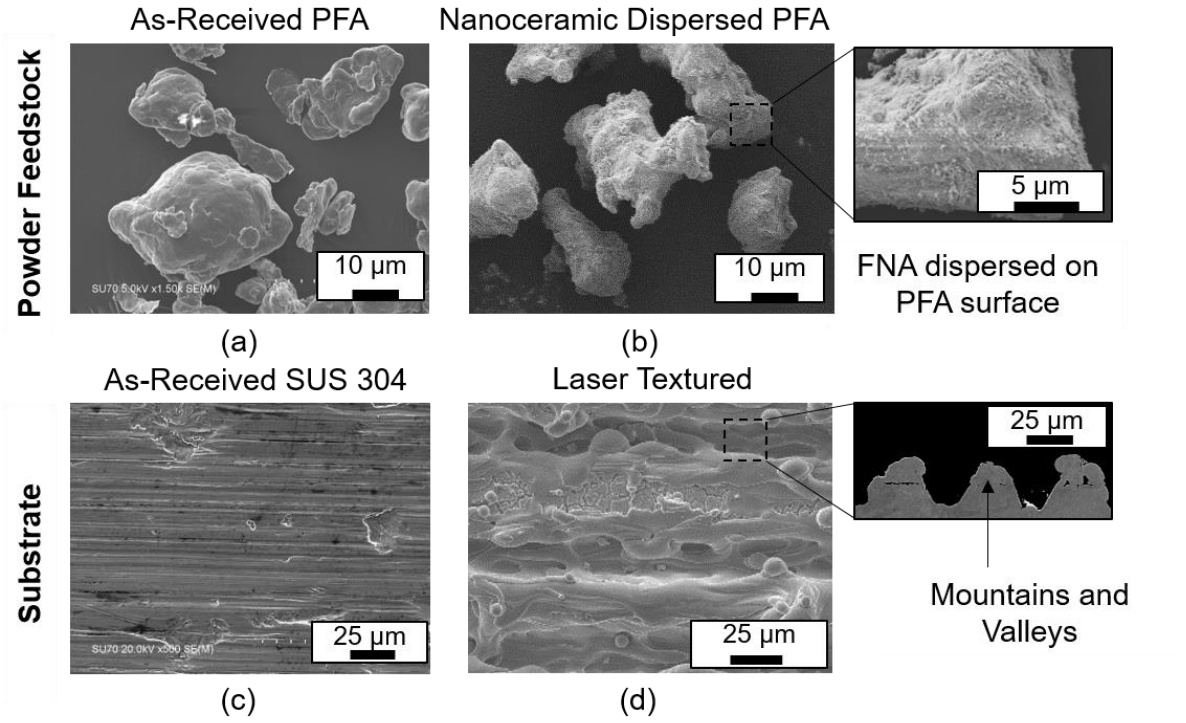
As-Received PFA
Nanoceramic Dispersed PFA
Powder Feedstock
10 μm
10 μm
5 μm
FNA dispersed on PFA surface
(a)
(b)
As-Received SUS 304
Laser Textured
Substrate
25 μm
25 μm
25 μm
Mountains and Valleys
(c)
(d)

1

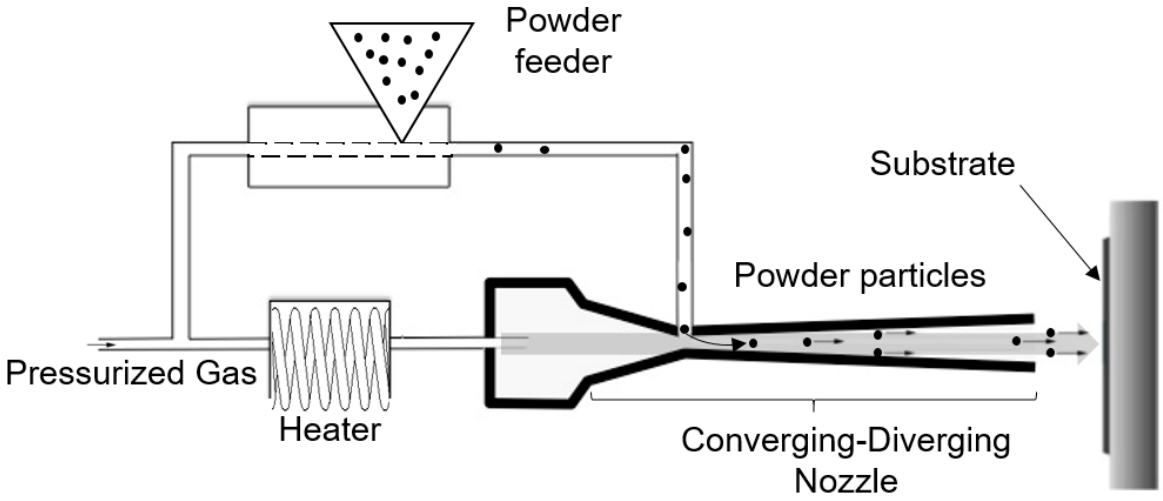
Powder feeder
Substrate
Powder particles
Pressurized Gas
Heater
Converging-Diverging Nozzle

2

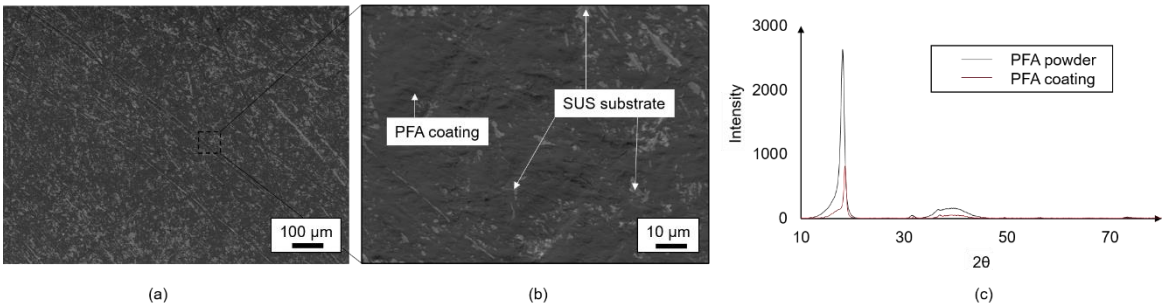
100 μm
PFA coating
SUS substrate
10 μm
3000
2000
1000
0
Intensity
10
30
50
70
2θ
PFA powder
PFA coating
(a)
(b)
(c)

3

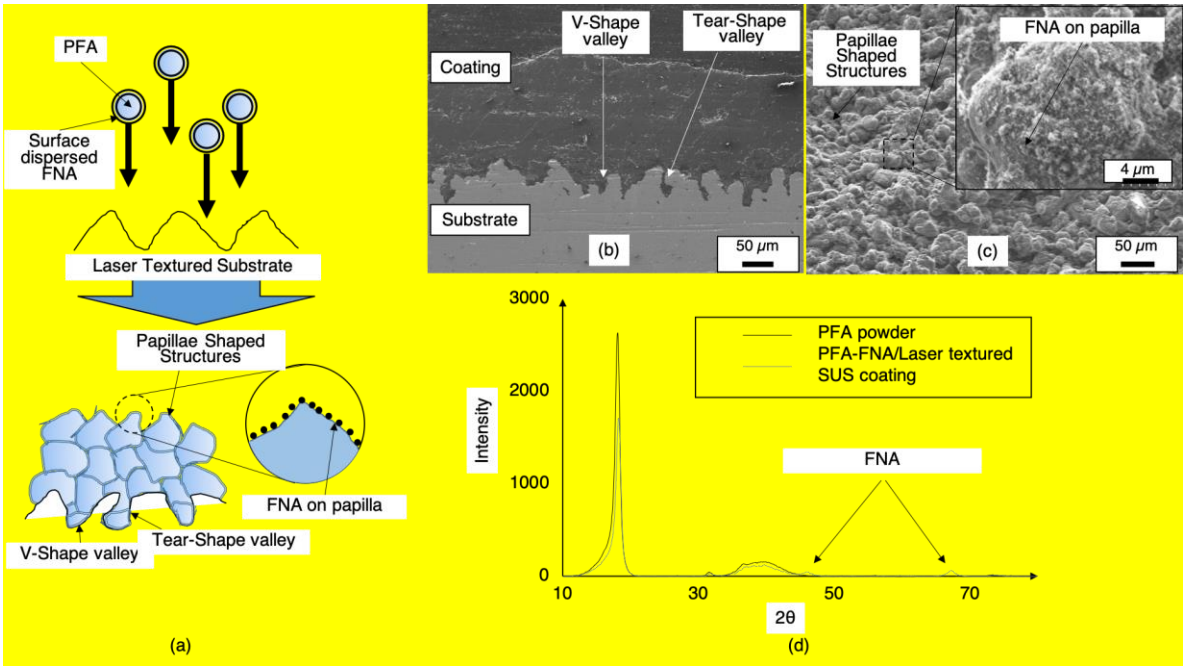
PFA
Surface dispersed FNA
Laser Textured Substrate
Papillae Shaped Structures
FNA on papilla
V-Shape valley
Tear-Shape valley
(a)
Coating
V-Shape valley
Tear-Shape valley
Substrate
(b)
50 μm
Papillae Shaped Structures
FNA on papilla
4 μm
(c)
50 μm
3000
2000
1000
0
Intensity
10
30
50
70
2θ
PFA powder
PFA-FNA/Laser textured
SUS coating
FNA
(d)

4

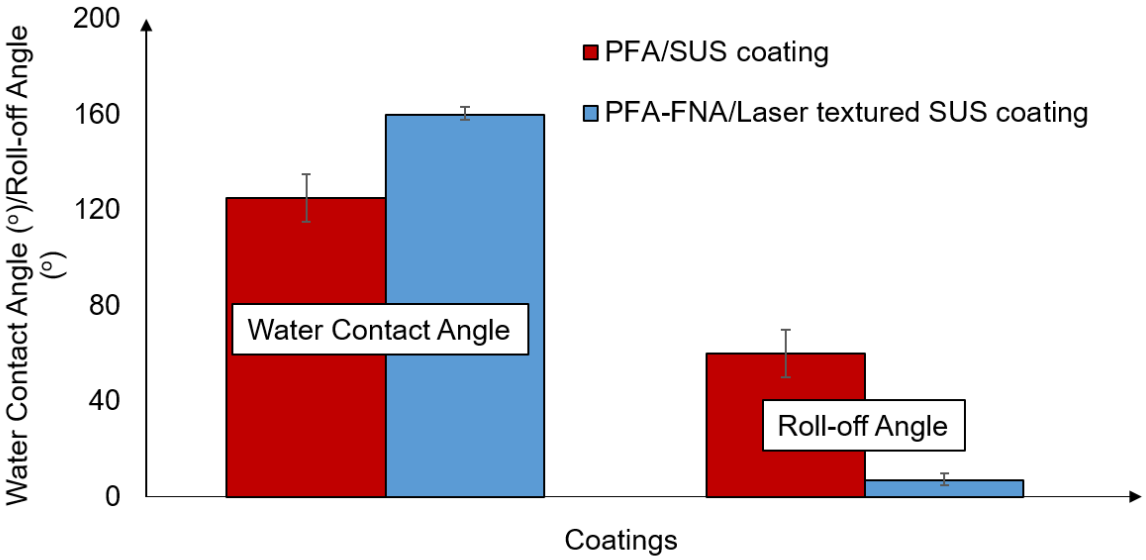
200
160
120
80
40
0
Water Contact Angle (°)/Roll-off Angle (°)
PFA/SUS coating
PFA-FNA/Laser textured SUS coating
Water Contact Angle
Roll-off Angle
Coatings

5

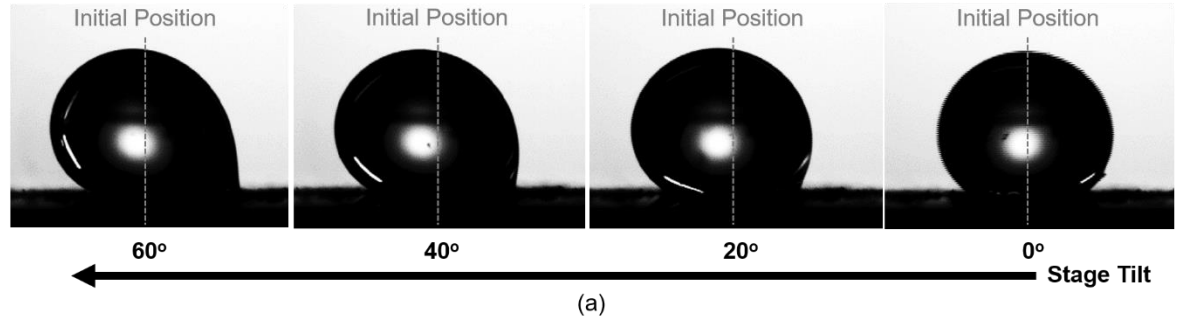
Initial Position
Initial Position
Initial Position
Initial Position
60°
40°
20°
0°
Stage Tilt

(a)

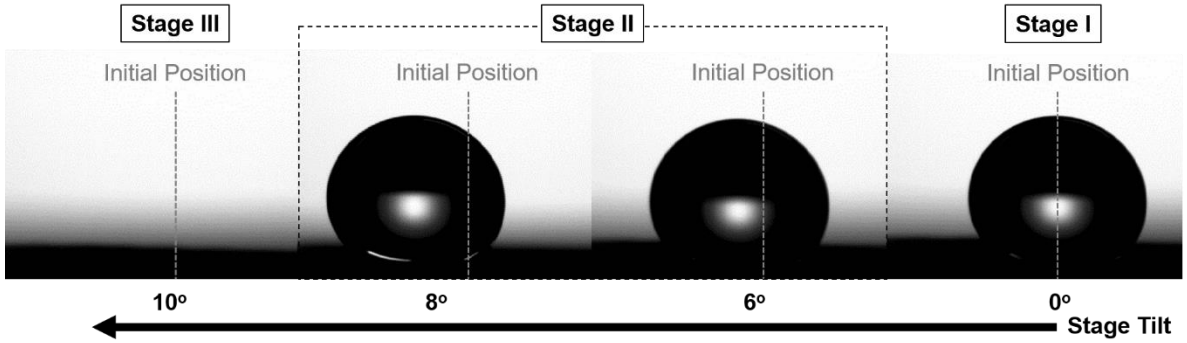
Stage III
Stage II
Stage I
Initial Position
Initial Position
Initial Position
Initial Position
10°
8°
6°
0°
Stage Tilt

(b)

6

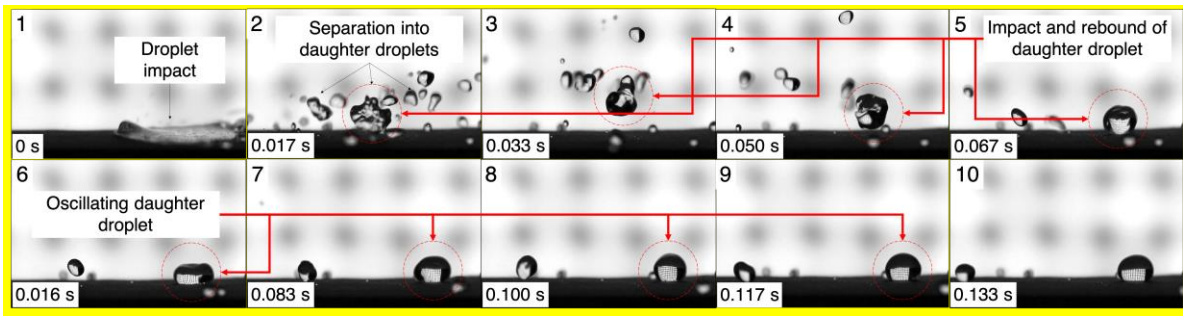
1
Droplet impact
0 s
2
Separation into daughter droplets
0.017 s
3
0.033 s
4
0.050 s
5
Impact and rebound of daughter droplet
0.067 s
6
Oscillating daughter droplet
0.016 s
7
0.083 s
8
0.100 s
9
0.117 s
10
0.133 s

7

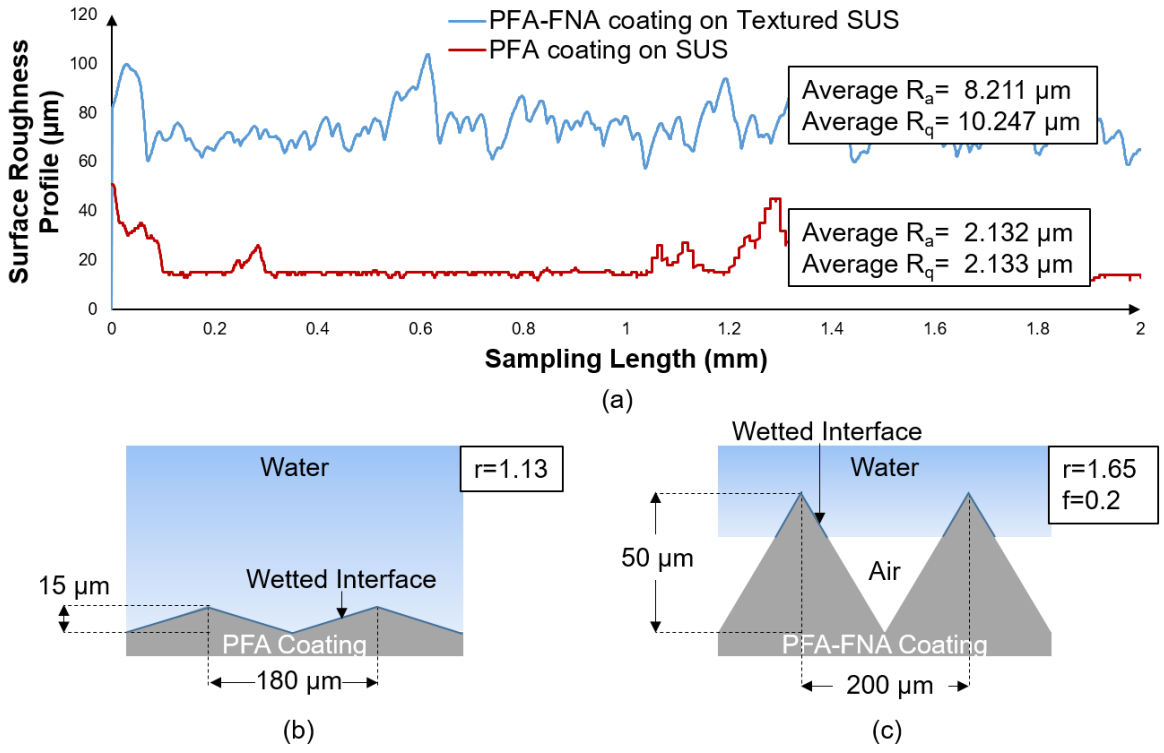
PFA-FNA coating on Textured SUS
PFA coating on SUS
Average Ra= 8.211 μm
Average Rq= 10.247 μm
Average Ra= 2.132 μm
Average Rq= 2.133 μm
Surface Roughness Profile (μm)
Sampling Length (mm)
(a)
Water
r=1.13
15 μm
Wetted Interface
PFA Coating
180 μm
(b)
Wetted Interface
Water
r=1.65
f=0.2
50 μm
Air
PFA-FNA Coating
200 μm
(c)

8

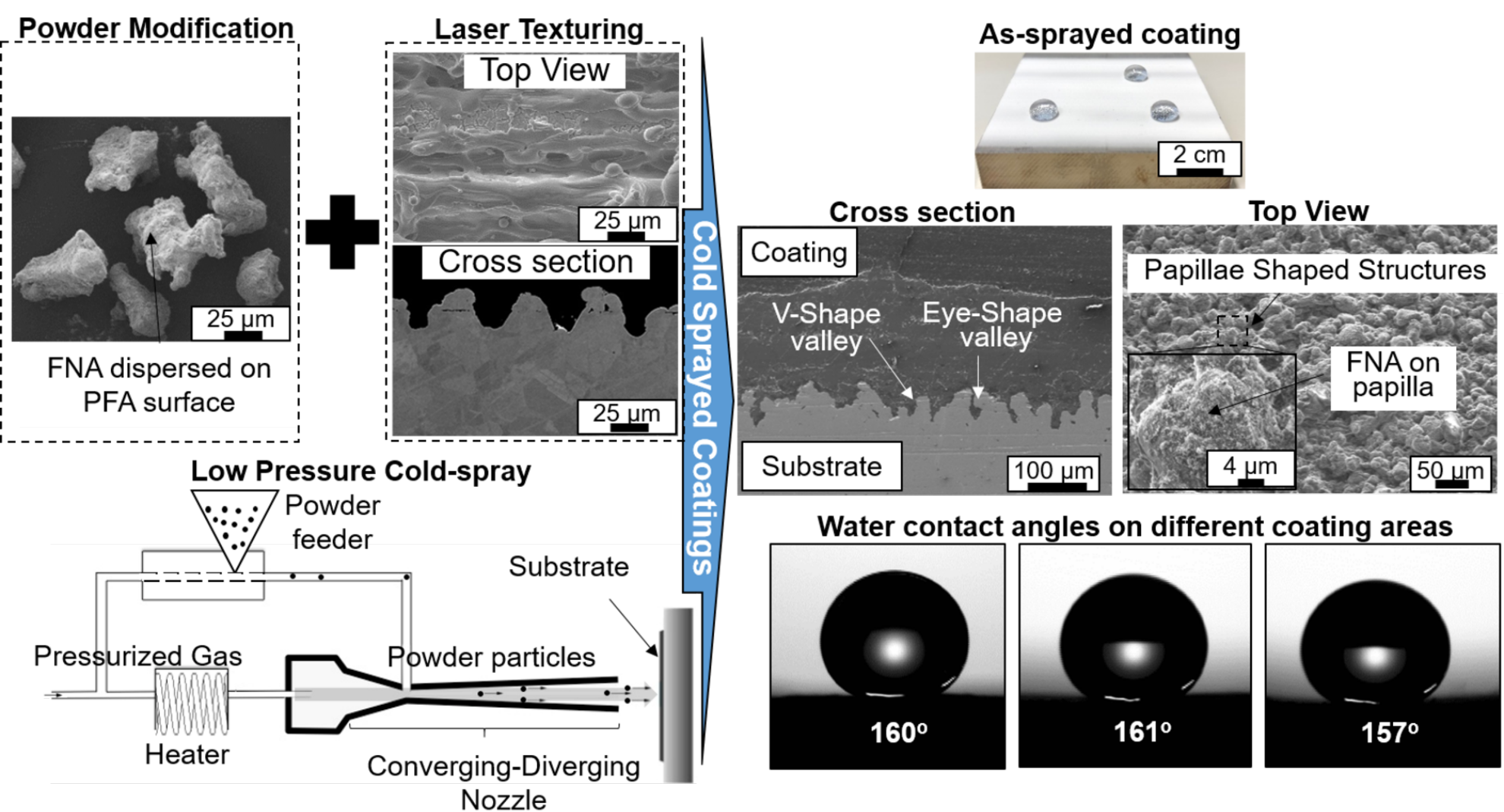
Powder Modification
25 µm
FNA dispersed on PFA surface
Laser Texturing
Top View
25 µm
Cross section
25 µm
Cold Sprayed Coatings
Low Pressure Cold-spray
Powder feeder
Substrate
Pressurized Gas
Powder particles
Heater
Converging-Diverging Nozzle
As-sprayed coating
2 cm
Cross section
Coating
V-Shape valley
Eye-Shape valley
Substrate
100 µm
Top View
Papillae Shaped Structures
FNA on papilla
4 µm
50 µm
Water contact angles on different coating areas
160°
161°
157°